Acta Pharmaceutica Sinica B 2025;15(10):5231−5243

Chinese Pharmaceutical Association
Institute of Materia Medica, Chinese Academy of Medical Sciences

Acta Pharmaceutica Sinica B

www.elsevier.com/locate/apsb
www.sciencedirect.com

ORIGINAL ARTICLE

Divergent activation patterns of BRS3 revealed by two Chinese herb-derived agonists

Jie Li[a,†], Changyao Li[b,c,d,†], Qingtong Zhou[e,†], Wei Han[e,†], Mingzhu Fang[f], Youwei Xu[b], Yiting Mai[g], Yao Zhang[a], Jiahua Cui[h], H. Eric Xu[b,c,e,i], Yan Zhang[f,*], Wanchao Yin[b,i,j,*], Ming-Wei Wang[a,e,g,k,l,*]

[a]*Department of Pharmacology, School of Basic Medical Sciences, Fudan University, Shanghai 200032, China*
[b]*State Key Laboratory of Drug Research, Shanghai Institute of Materia Medica, Chinese Academy of Sciences, Shanghai 201203, China*
[c]*School of Life Science and Technology, ShanghaiTech University, Shanghai 201210, China*
[d]*Lingang Laboratory, Shanghai 200031, China*
[e]*Research Center for Medicinal Structural Biology, National Research Center for Translational Medicine at Shanghai, State Key Laboratory of Medical Genomics, Ruijin Hospital, Shanghai Jiao Tong University School of Medicine, Shanghai 200025, China*
[f]*Shanghai Frontiers Science Center of Drug Target Identification and Delivery, School of Pharmaceutical Sciences, Shanghai Jiao Tong University, Shanghai 200240, China*
[g]*Research Center for Deepsea Bioresources, Sanya 572025, China*
[h]*School of Chemistry and Chemical Engineering, Shanghai Jiao Tong University, Shanghai 200240, China*
[i]*University of Chinese Academy of Sciences, Beijing 100049, China*
[j]*Zhongshan Institute for Drug Discovery, Shanghai Institute of Materia Medica, Chinese Academy of Sciences, Zhongshan 528400, China*
[k]*Engineering Research Center of Tropical Medicine Innovation and Transformation of Ministry of Education, School of Pharmacy, Hainan Medical University, Haikou 570228, China*
[l]*Department of Chemistry, School of Science, the University of Tokyo, Tokyo 113-0033, Japan*

Received 25 February 2025; received in revised form 9 May 2025; accepted 6 June 2025

*Corresponding authors.
E-mail addresses: zhangyan_sjtu@sjtu.edu.cn (Yan Zhang), wcyin@simm.ac.cn (Wanchao Yin), mwwang@simm.ac.cn (Ming-Wei Wang).
[†]These authors made equal contributions to this work.

Peer review under the responsibility of Chinese Pharmaceutical Association and Institute of Materia Medica, Chinese Academy of Medical Sciences.

https://doi.org/10.1016/j.apsb.2025.06.025

KEY WORDS

Bombesin receptor subtype-3;
Cryo-EM;
Structural pharmacology;
Unliganded;
Chinese herb DSO-5a;
Oridonin;
Receptor activation;
Drug discovery

Abstract Bombesin receptor subtype-3 (BRS3) is an orphan G protein-coupled receptor (GPCR) that plays critical roles in energy homeostasis, glucose metabolism, and insulin secretion. Recent structural studies have elucidated BRS3 signaling mechanisms using synthetic ligands, including BA1 and MK-5046. However, the molecular basis of BRS3 activation by bioactive natural compounds and their derivatives, particularly those derived from traditional Chinese medicine, remains unclear. Here, we present high-resolution cryogenic electron microscopy (cryo-EM) structures of the human BRS3−G_q complex in both unliganded and active states bound by two herb-derived compounds (DSO-5a and oridonin), at resolutions of 2.9, 2.8, and 2.9 Å, respectively. These structures display distinct ligand recognition patterns between DSO-5a and oridonin. Although both compounds bind to the orthosteric pocket, they differentially engage the interaction network of BRS3, as demonstrated by mutagenesis studies assessing calcium mobilization and inositol phosphate 1 (IP1) accumulation. These findings enhance our understanding of BRS3 activation and provide valuable insights into the development of small-molecule BRS3 modulators with therapeutic potential.

1. Introduction

Bombesin receptor subtype-3 (BRS3), an orphan G protein-coupled receptor (GPCR) predominantly expressed in the hypothalamus and pancreatic β-cells[1,2], plays pivotal roles in regulating energy homeostasis, glucose metabolism, and insulin secretion[3-5]. Through adaptive evolution, placental mammalian BRS3 has undergone positive selection, acquiring constitutive G_s, G_q, and G_{12} signaling activity independent of ligand binding[6]. Studies involving BRS3-deficient mice have confirmed its essential function in maintaining energy balance. Activation of BRS3-expressing neurons in the hypothalamus by various stimuli leads to region-specific physiological responses. For instance, BRS3 activation in the dorsomedial hypothalamus increases energy expenditure and sympathetic tone without affecting food intake, whereas activation in the paraventricular nucleus reduces food intake without impacting energy expenditure[7]. Additionally, BRS3 agonists have been shown to stimulate insulin secretion from pancreatic β-cells, highlighting BRS3 as a potential drug target for metabolic diseases[8]. However, the molecular mechanisms underlying BRS3 signaling remain elusive.

Traditional Chinese medicine (TCM) has long served as a valuable and rich source of bioactive substances[9]. Recent studies discovered two compounds derived from TCM, DSO-5a and oridonin, as novel BRS3 agonists[10,11]. DSO-5a is a representative optimized derivative of shikonin, an enantiomer extracted and characterized from the roots of *Lithospermum erythrorhizon* (Fig. 1A)[11-13]. It has been demonstrated to upregulate the peroxisome proliferator-activated receptor-gamma (PPAR-γ) activity and enhance the extracellular signal-regulated kinase 1/2 (ERK1/2) phosphorylation through BRS3 signaling[11]. Unlike previously reported BRS3 agonists that often affect both central and peripheral systems[14], DSO-5a selectively activates peripheral BRS3 to regulate blood glucose effectively while minimizing central side effects[11,14]. Oridonin, a diterpenoid isolated from *Isodon rubescens* (Fig. 1B)[15], exhibits broader pharmacological properties, including hypoglycemic[16], anti-inflammatory[17,18], and anti-cancer effects[19]. It was later identified as a BRS3 ligand[10]. The cryogenic electron microscopy (cryo-EM) structures of BRS3 bound by two synthetic compounds, BA1 (a pan bombesin receptor agonist) and MK-5046 (a BRS3-specific agonist), were reported recently, providing valuable insights into ligand recognition by BRS3[20].

In this study, we present high-resolution cryo-EM structures of the human BRS3−G_q complex in both unliganded and active states bound by DSO-5a and oridonin at resolutions of 2.9, 2.8, and 2.9 Å, respectively. These structures offer valuable insights into the distinct ligand recognition patterns and BRS3 activation mechanisms by Chinese herb-derived agonists.

2. Methods

2.1. Cell culture

Spodoptera frugiperda (*Sf*9) and *Trichoplusia ni* (High Five™) insect cells (Expression Systems, Davis, CA, USA) were cultured in ESF 921 insect cell culture medium (Expression Systems) at 27 °C and 120 rpm (Infors HT, Bottmingen, Switzerland). HEK293T cells were grown in Dulbecco's modified Eagle's medium (DMEM, Life Technologies, Carlsbad, CA, USA) supplemented with 10% fetal bovine serum (FBS, Gibco, Carlsbad, CA, USA) at 37 °C in 5% CO_2 humidified incubator (ThermoFisher Scientific, Waltham, MA, USA).

2.2. Construct

For expression of the unliganded BRS3−G_q and DSO-5a−BRS3−G_q complexes, a hemagglutinin (HA) signal peptide was added to the N terminus of the human BRS3 (residues 1−399). In the oridonin−BRS3−G_q complex, an additional BRIL[21] sequence was introduced. To ensure complex stability and homogeneity, the NanoBiT tethering strategy was employed[22,23], in which the C terminus of BRS3 was directly attached to the LgBiT subunit (Promega, Madison, WI, USA), followed by a tobacco etch virus (TEV) protease cleavage site and a 8 × His tag or a double maltose binding protein (MBP) tag (Supporting Information Fig. S1A). The C terminus of rat Gβ1 was linked to peptide 86 subunit[22,23] (also named as HiBiT, Promega) with a 15-amino acid polypeptide (GSSGGGGSGGGGSSG) linker. An engineered Gα_q construct[24] was utilized for expression and purification of the unliganded BRS3−G_q and DSO-5a−BRS3−G_q

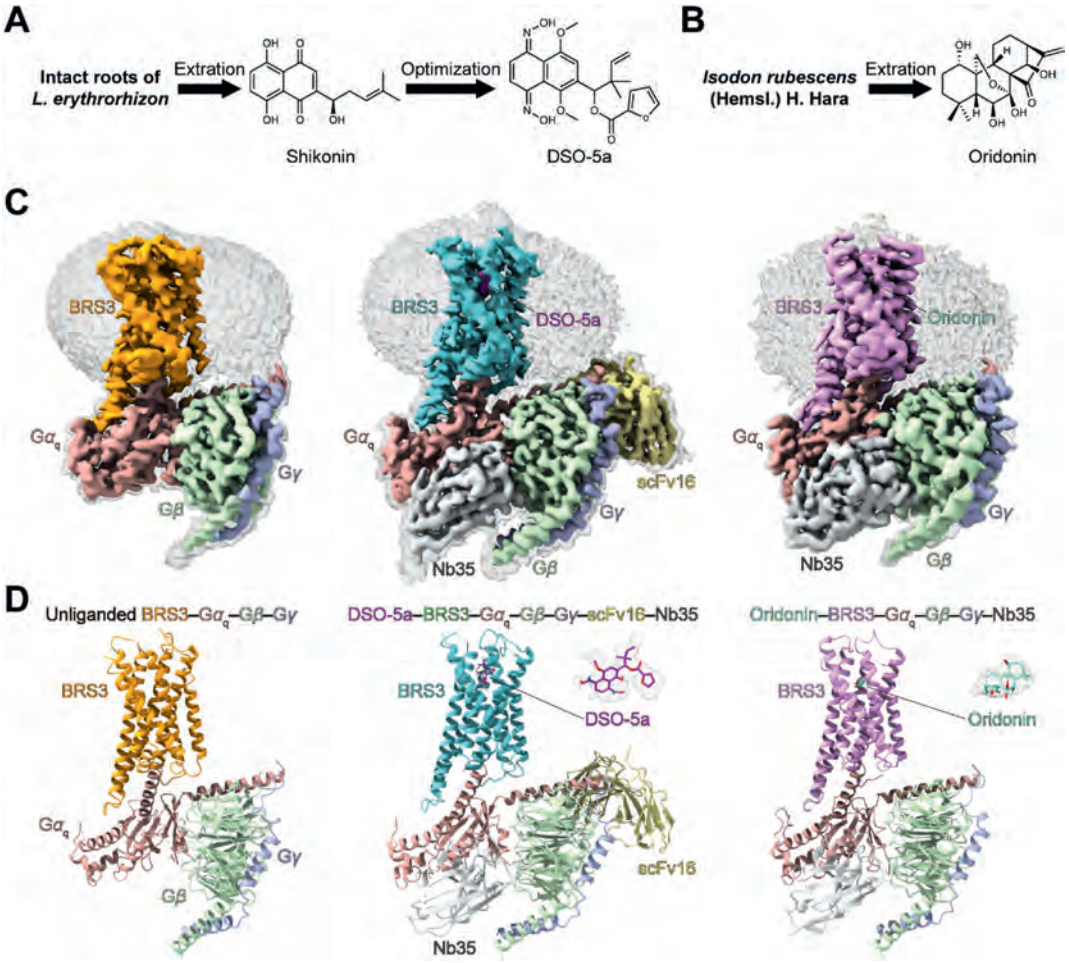

Figure 1 Cryo-EM structures of the unliganded, DSO-5a-bound and oridonin-bound BRS3−G_q complexes. (A, B) Origin and chemical structures of DSO-5a (A) and oridonin (B). (C, D) Cryo-EM density map (C) and corresponding structure model (D) of the unliganded (left), DSO-5a-bound (middle) and oridonin-bound (right) BRS3−G_q complexes.

complexes. For the oridonin−BRS3−G_q complex, a modified $G\alpha_q$ construct was generated based on mini-$G_{s/q}$71[25], which carries two dominant-negative mutations (G203A and A326S)[26] to decrease nucleotide binding affinity and facilitate $G\alpha\beta\gamma$ complex stability. The N-terminal 1−18 amino acids and the α-helical domain of the mini-$G_{s/q}$71 were substituted with the corresponding sequences of the human $G\alpha_{i1}$ to enable binding to the antibody fragments scFv16[27,28]. The antibody fragment scFv16, containing an N-terminal GP67 secretion signal peptide, was used to stabilize the nucleotide-free BRS3−G_q complex. The constructs were cloned into both pcDNA3.1 and pFastBac vectors for functional assays in mammalian cells and protein expression in insect cells, respectively.

2.3. *Nanobody 35*

Nanobody 35 (Nb35) with a C-terminal 6 × His-tag was expressed in the periplasm of *E. coli* BL21 (DE3) and purified by nickel affinity chromatography as previously described[29]. Briefly, the Nb35 gene was transformed into BL21 (DE3) and grown in a TB culture medium with 100 μg/mL ampicillin, 2 mmol/L $MgCl_2$, and 0.1% (*w*/*v*) glucose at 37 °C, 180 rpm (Jinghong, Shanghai, China). Then the expression was induced by adding 1 mmol/L IPTG when OD_{600} reached 0.7−1.2. After overnight incubation at 28 °C and 180 rpm, the cell pellet was collected by centrifugation and stored at −80 °C until use. The HiLoad 16/600 Superdex 75 column (GE Healthcare, Chicago, IL, USA) was used to separate the monomeric fractions of Nb35 with a running buffer (pH 7.5) containing 20 mmol/L HEPES and 100 mmol/L NaCl. The purified Nb35 containing 30% (*v*/*v*) glycerol was flash-frozen by liquid nitrogen and stored at −80 °C until use.

2.4. *Expression and purification*

The Bac-to-Bac Baculovirus Expression System (Invitrogen, Carlsbad, CA, USA) was used to generate high titer recombinant baculovirus for BRS3-LgBiT, $G\alpha_q$, $G\beta$1-HiBiT, $G\gamma$2 and scFv16. P0 viral stock was produced by transfecting 5 μg recombinant bacmids into *Sf*9 cells (2.5 mL, density of 1 million cells per mL) for 96 h incubation and then used to produce P1 and P2 baculoviruses. The BRS3-LgBiT, $G\alpha_q$, $G\beta$1-HiBiT, $G\gamma$2 and scFv16 were co-expressed at multiplicity of infection (MOI) ratio of 1:1:1:1:1 by infecting *Sf*9 (for the unliganded BRS3−G_q and DSO-5a−BRS3−G_q complexes) or High Five cells (for the oridonin−BRS3−G_q complex) at a density of 3 million cells per mL with P2 baculovirus (viral titer >90%). The culture was harvested

by centrifugation 48 h post-infection, and cell pellets were stored at −80 °C until use.

The cell pellets were thawed and lysed in a buffer containing 20 mmol/L HEPES, pH 7.5, 100 mmol/L NaCl, 10% (*v*/*v*) glycerol, 10 mmol/L $MgCl_2$, 1 mmol/L $MnCl_2$, and 100 μmol/L TCEP (Sigma−Aldrich, St. Louis, MO, USA) supplemented with EDTA-free protease inhibitor cocktail (TargetMol, Boston, MA, USA) by dounce homogenization. The unliganded BRS3−G_q complex formation was initiated by the addition of 10 μg/mL Nb35 and 25 mU/mL apyrase (New England Bio-Labs, Beverly, MA, USA). For the DSO-5a−BRS3−G_q and oridonin-BRS3-G_q complex formation, additional 50 μmol/L DSO-5a (Supporting Information Fig. S2)[11] and 1 mmol/L oridonin (ChemFaces, Wuhan, China) were added, respectively.

For the oridonin−BRS3−G_q complex, the subsequent solubilization, purification and gel filtration steps followed the same protocol as described for the BA1−BRS3−G_q complex, maintaining 1 mmol/L oridonin throughout the purification process[20]. For the unliganded BRS3−G_q and DSO-5a−BRS3−G_q complexes, after incubation at room temperature (RT) for 1.5 h, the membrane was solubilized in the buffer above supplemented with 0.5% (*w*/*v*) lauryl maltose neopentyl glycol (LMNG, Anatrace, Maumee, OH, USA) and 0.1% (*w*/*v*) cholesterol hemisuccinate (CHS, Anatrace) for 2 h at 4 °C. The supernatant was isolated by centrifugation at 65,000×*g* for 30 min and incubated with Ni NTA Beads 6FF (Smart-Lifesciences, Changzhou, China) for 2 h at 4 °C. The resin was then collected by centrifugation at 600×*g* for 10 min and washed in gravity flow column (Sangon Biotech, Shanghai, China) with five column volumes of wash buffer [pH 7.5, 20 mmol/L HEPES, 100 mmol/L NaCl, 10% (*v*/*v*) glycerol, 5 mmol/L $MgCl_2$ and 1 mmol/L $MnCl_2$] containing 30 mmol/L imidazole, 25 μmol/L TCEP, 0.1% (*w*/*v*) LMNG, 0.02% (*w*/*v*) CHS and 10 μmol/L ligand. A subsequent wash was conducted with fifteen column volumes of wash buffer containing 60 mmol/L imidazole, 25 μmol/L TCEP, 0.03% (*w*/*v*) LMNG, 0.01% (*w*/*v*) glyco-diosgenin (GDN, Anatrace), 0.008% (*w*/*v*) CHS and 10 μmol/L ligand.

The protein was then eluted with five column volumes of wash buffer containing 300 mmol/L imidazole, 25 μmol/L TCEP, 0.03% (*w*/*v*) LMNG, 0.01% (*w*/*v*) glyco-diosgenin (GDN, Anatrace), 0.008% (*w*/*v*) CHS and 10 μmol/L ligand. The flow-through was collected and concentrated with a Amicon Ultra centrifugal filter (molecular weight cut-off of 100 kDa, Merk Millipore, Billerica, MA, USA) and then subjected to a Superdex 200 Increase 10/300 GL column (GE Healthcare) with a running buffer (pH 7.5) containing 20 mmol/L HEPES, 100 mmol/L NaCl, 10 mmol/L $MgCl_2$, 100 μmol/L TCEP, 10 μmol/L ligand, 0.00075% (*w*/*v*) LMNG, 0.00025% (*w*/*v*) GDN and 0.0002% (*w*/*v*) CHS. The fractions of the monomeric complex were collected and concentrated to 10 mg/mL for electron microscopy examination.

2.5. Cryo-EM data acquisition

The purified sample (3 μL) was applied to glow-discharged holey carbon grids (Quantifoil R1.2/1.3, 300 mesh), and subsequently vitrified using a Vitrobot Mark IV (ThermoFisher Scientific) set at 100% humidity and 4 °C. For the unliganded BRS3−G_q and DSO-5a−BRS3−G_q complexes, cryo-EM images were collected on a Titan Krios microscope (FEI, ThermoFisher Scientific) equipped with a Gatan energy filter and K3 direct electron detector and performed using serialEM. The microscope was operated at 300 kV accelerating voltage and a calibrated magnification of × 81,000 corresponding to a pixel size of 1.071 Å. An accumulated dose of 80 electrons per $Å^2$ was fractionated into a movie stack of 36 frames, with a defocus range of −1.2 to −2.2 μm. A total of 3519 images for the unliganded BRS3−G_q complex and 6683 images for the DSO-5a−BRS3−G_q complex were collected. For the oridonin−BRS3−G_q complex, the data were collected on a Titan Krios microscope equipped with a Falcon4 direct electron detector (ThermoFisher Scientific) at 300 kV with a magnification of × 165,000, corresponding to a pixel size of 0.73 Å. A total of 8180 movies were collected using EPU Software, with a total dose of 50 $e^-/Å^2$ over 2.5 s exposure on each EER format movie. Each movie was divided into 36 frames during motion correction.

2.6. Cryo-EM data processing

For the unliganded BRS3−G_q complex, the micrographs were processed using cryoSPARC v.4.4.121 with patch motion correction to restore the correct information of the original cryo-EM images (Supporting Information Fig. S3). The contrast transfer function (CTF) parameters were estimated using patch CTF estimation. Template picking referenced from the cryo-EM map of the GRP14-27−GRPR−G_q (EMDB code: EMD-34414)[30] yielded 4,216,264 particle projections, which were subjected to two rounds of two-dimensional (2D) classification to discard false positive particles or particles categorized in poorly defined classes, producing 2,160,205 particle projections. The *ab-initio* reconstruction and hetero refinement were applied to divide particles into five subsets, a selected subset of 1,156,480 particle projections was subjected to further processing. To improve the density quality of specific regions, this subset of particle projections was subjected to three-dimensional (3D) auto-refinement with a mask on the complex, which was subsequently subjected to another round of 3D classifications with a mask on the ECD. After the last round of non-uniform (NU) refinement, the final map of the unliganded BRS3−G_q complex has an indicated global resolution of 2.93 Å by the 0.143 criteria of the gold-standard Fourier shell correlation (FSC), based on a dataset of 693,649 particles.

For the DSO-5a−BRS3−G_q complex (Fig. S3), 6683 movies were motion corrected and CTF estimated, and 7,422,677 particles were auto-picked by template picker referenced to the unliganded BRS3−G_q map we obtained. After two rounds of 2D classification, four rounds of 3D classification and hetero refinement, and one round of NU refinement and local refinement, 238,182 particles were used to generate a map with an indicated global resolution of 2.83 Å at an FSC of 0.143. For datasets of the oridonin−BRS3−G_q complex, the similar strategy was employed (Fig. S3). After NU refinement, 179,257 particles were reconstructed to a 2.94 Å map at an FSC of 0.143.

2.7. Model building and refinement

The cryo-EM structure of the GRP14-27−GRPR−G_q (PDB code: 8H0Q)[30] was employed as the initial structure template for modeling the unliganded form, DSO-5a-bound and oridonin-bound BRS3−G_q complexes. The initial models were fitted to the EM density map using the UCSF Chimera 1.17.3[31,32], followed by interactive rounds of manual adjustment and automated refinement in COOT 0.9.8.92[33] and Phenix 1.21[34], respectively (Supporting Information Fig. S4). The final refinement statistics were validated using the module comprehensive validation (cryo-EM) in Phenix 1.21. Structural Figures were prepared in UCSF Chimera 1.17.3, UCSF ChimeraX v1.0 and PyMOL 2.5.8 (https://

pymol.org/2/). The final refinement statistics are provided in Supporting Information Table S1.

2.8. IP1 accumulation assay

Accumulation of IP1 was measured using the IP-One HTRF kit (Cisbio, Codolet, France). Briefly, HEK293 cells were seeded onto 12-well plates and cultured for 16 h before transfection. BRS3 constructs were transiently transfected into the cells using FuGENE HD transfection reagent (Promega, Madison, WI, USA). After 24 h, cells were harvested, resuspended in IP1 stimulation buffer, and then distributed into 384-well assay plates (4900 cells/7 μL/well). An equal volume (7 μL) of IP1 Stimulation Buffer 2 containing a given ligand was added to each well, followed by incubation at 37 °C for 1 h. Intracellular IP1 levels were then measured using the IP-One HTRF kit (PerkinElmer, Waltham, MA, USA) on an EnVision multiplate reader (PerkinElmer) following the manufacturer's instructions.

2.9. Calcium mobilization assay

Calcium mobilization in response to DSO-5a and oridonin was determined using HEK293T cells transfected with the human BRS3. Cells were seeded onto 6-well plates, cultured overnight until reaching 80% confluence, and then transfected with WT or mutant BRS3 plasmids using Lipofectamine 2000 (Invitrogen) according to the manufacturer's protocol. After 24 h, transfected cells were reseeded into black, clear-bottom 384-well plates at 20,000 cells per well in 25 μL of DMEM with 10% FBS. The next day, cells were loaded with Calcium 6 dye (Molecular Devices, San Jose, CA, USA; diluted in HBSS containing 20 mmol/L HEPES, pH 7.4) and incubated at 37 °C in darkness for 2 h. Compound solutions (5 × final concentration in HBSS with 20 mmol/L HEPES and 0.1% BSA, pH 7.4) were added using the FLIPR Penta system (Molecular Devices). Baseline fluorescence was recorded for 10 s (1 read/s), followed by compound addition and fluorescence measurement for 50 s (1 read/s). The maximum fold-change in fluorescence was calculated as the ratio of the peak fluorescence (within 50 s post-addition) to the average baseline fluorescence, and data were normalized to the percentage of maximal stimulation in WT BRS3 receptor-transfected cells.

2.10. Cell surface expression

The cell surface expression of each BRS3 mutant was assessed by fluorescence-activated cell sorting (FACS) analysis. The mutant constructs were cloned into pcDNA3.1 vector (Invitrogen) with an N-terminal FLAG tag. HEK293T cells were seeded onto 6-well plates and transfected following the same protocol as described in the calcium mobilization assay. After 24 h of transfection, cells were washed with PBS and detached using 0.2% (*w*/*v*) EDTA in PBS. Subsequently, cells were blocked with PBS containing 5% BSA (*w*/*v*) at RT for 15 min, followed by incubation with monoclonal PE anti-DYKDDDDK Tag antibody (Biolegend, San Diego, CA, USA) at a 1:100 dilution in PBS containing 5% BSA for 1 h at 4 °C. After incubation, cells were washed three times with PBS containing 1% BSA (*w*/*v*) and resuspended in PBS. Fluorescence intensity was quantified using a Guava® easyCyte™ flow cytometer (Cytek Biosciences, Fremont, CA, USA). Data were analyzed and normalized to the WT BRS3 expression levels (Supporting Information Table S2).

2.11. Molecular dynamics (MD) simulation

MD simulations were performed by Gromacs 2021.4[35]. The MD simulation of the DSO-5a —bound BRS3 was built based on the cryo-EM structure and prepared by the Protein Preparation Wizard (Schrödinger 2023-2)[36]. The protein chain termini were capped with acetyl and methylamide. All titratable residues were left in their dominant state at pH 7.0. To build MD simulation systems, the complexes were embedded in solvated with 0.15 mol/L NaCl in explicit TIP3P waters using CHARMM-GUI Solution Builder[37]. The CHARMM36m force field[38] was adopted for protein and salt ions. The parameter of DSO-5a was generated using the CHARMM General Force Field (CGenFF)[39]. The Particle Mesh Ewald (PME) method was used to treat all electrostatic interactions beyond a cut-off of 12 Å and the bonds involving hydrogen atoms were constrained using LINCS algorithm[40]. The complex system was first relaxed using the steepest descent energy minimization, followed by slow heating of the system to 310 K with restraints. The restraints were reduced gradually over 10 ns. Finally, restrain-free production run was carried out for each simulation, with a time step of 2 fs in the NPT ensemble at 310 K and 1.0 bar using the V-rescale thermostat and the isotropic Parrinello-Rahman barostat[41], respectively. Similar simulation procedure and analysis were adopted for the MD simulations of unliganded NMB-bound, DSO-5a-bound, and oridonin-bound BRS3 complex. The interface areas of agonist-receptor were calculated by FreeSASA using the Sharke-Rupley algorithm with a probe radius of 1.2 Å.

2.12. Statistical analysis

All functional study data were analyzed using Prism 10 (GraphPad, San Diego, CA, USA) and presented as mean ± standard error of mean (SEM) from at least three independent experiments. Concentration-response curves were evaluated with a three-parameter logistic equation. The significance was determined with one-way ANOVA or Kruskal−Wallis test, and $P < 0.05$ was considered statistically significant.

3. Results

3.1. Structure determination

To prepare high-quality BRS3−G_q complexes, the thermostabilized apocytochrome b^{562}RIL (BRIL) and the NanoBiT tethering strategy were employed (Fig. S1A)[21-23]. The BRS3−G_q complexes were assembled by co-expressing and subsequently purified as monodispersed peaks *via* size exclusion chromatography (SEC) demonstrating good homogeneity. SDS-PAGE analysis confirmed the presence of all the expected components (Fig. S1B−S1D). After sample preparation, cryo-EM data collection, and analysis, three-dimensional (3D) consensus density maps were reconstructed, achieving overall resolutions of 2.9, 2.8 and 2.9 Å for the unliganded, DSO-5a-bound and oridonin-bound BRS3−G_q complexes, respectively (Fig. S3 and Table S1).

These cryo-EM maps enabled near-atomic modeling for most regions of the complexes, except for the stalk between transmembrane helix 1 (TM1) and the N terminus of BRS3 (Fig. S4). Both DSO-5a and oridonin were clearly resolved in the cryo-EM maps, allowing for precise structural modeling of the backbones and side chains of most residues (Fig. 1). Structural superposition

revealed that the three receptor structures exhibited highly similar overall conformations, with Cα root-mean-square deviation (RMSD) values ranging from 0.79 to 1.22 Å, indicating that both compounds stabilize the active conformation in a similar manner.

3.2. Unliganded architecture

The cryo-EM structure of the unliganded BRS3−G_q complex was determined without the intentional addition of exogenous ligands (*i.e.*, 'unliganded'), although unintentional ligand introduction from the experimental system cannot be excluded. Despite the absence of an added agonist, the overall resolution of 2.9 Å is comparable to those of DSO-5a-bound and oridonin-bound BRS3−G_q complexes. Notably, the G protein and the lower half of the transmembrane domain of BRS3 exhibit relatively higher resolution features, whereas the extracellular half of BRS3 appears more dynamic (Fig. S3). The cryo-EM structure of the unliganded BRS3 closely resembles those of MK-5046-bound, DSO-5a-bound, and oridonin-bound BRS3, with Cα RMSD values of 0.94, 0.94, and 0.96 Å, respectively (Supporting Information Fig. S5). The intracellular regions are highly similar, suggesting minimal conformational change in the G protein-binding interface. Of note, in contrast to the DSO-5a-bound and oridonin-bound BRS3−G_q complexes, the cryo-EM densities for Nb35 or scFv16 were not observed, indicating weak binding of these two proteins in the unliganded state (Fig. 1C and D).

3.3. Recognition of DSO-5a

Structural superimposition reveals that the binding of DSO-5a is well overlapped with that of MK-5046, with a Cα RMSD of 1.28 Å (Fig. S5). In comparison with the unliganded structure, DSO-5a induces a modest outward shift of TM2 and TM7, with displacements of 1.6 and 3.0 Å, as measurement by the Cα atoms of $Y108^{2.65}$ and $M307^{7.29}$, respectively (Fig. 2). DSO-5a adopts a "Y"-shaped conformation and binds at the bottom of the BRS3 orthosteric binding pocket, situated within the upper half of the transmembrane domain, forming extensive polar and nonpolar contacts (Fig. 2A and B)[20].

Specifically, the dimethyl shikonin backbone of DSO-5a forms both polar and stacking interactions with residues in TM3 ($R127^{3.32}$), TM5 ($Q214^{5.35}$ *via* hydrogen bond and $H217^{5.38}$ *via* stacking), TM6 ($Y291^{6.55}$ *via* stacking) and $S205^{ECL2}$. $R127^{3.32}$ flips upward and engages in cation−π interactions with both the shikonin backbone and furan moiety of DSO-5a (Fig. 2C). Mutating $R127^{3.32}$ to alanine completely abolishes DSO-5a-induced Ca^{2+} mobilization as well as IP1 accumulation (Fig. 2D and Supporting Information Fig. S6, and Supporting Information Table S3). A similar loss of signaling was observed with the $Y291^{6.55}$A mutation, further highlighting their key roles in DSO-5a agonism. Mutations in other residues involved in polar interactions with DSO-5a significantly affect BRS3 signaling. In the Ca^{2+} mobilization assay, mutations $Q214^{5.35}$A and $H217^{5.38}$A result in a decrease in both the potency (EC_{50}, by 7.9- and 3.2-fold, respectively) and efficacy [E_{max}, decreasing from 100% in wild-type (WT) to 46.85% and 39.70%, respectively] of DSO-5a (Fig. 2D and Table S3). Similarly, in the IP1 accumulation assay, the same mutations cause a significant decline in potency (EC_{50}, by 3.7- and 2.3-fold, respectively) and efficacy (E_{max}, decreasing from 100% in WT to 50.32% and 72.96%, respectively; Fig. S6 and Table S3). Besides, DSO-5a establishes hydrogen bonds with $S205^{ECL2}$. Consistently, the $S205^{ECL2}$A reduces DSO-5a-induced signaling (Fig. 2D, Fig. S6, and Table S3).

In addition, the furan and β,β-dimethyl-γ-butylene groups of DSO-5a contribute notable contacts to receptor activation. The furan moiety forms hydrogen bonds with $N287^{6.51}$ and $R316^{7.39}$, and mutations $N287^{6.51}$A and $R316^{7.39}$A significantly reduce DSO-5a-induced Ca^{2+} mobilization and IP1 accumulation (Fig. 2D and Fig. S6, and Table S3). Extensive hydrophobic contacts are observed with residues in TM2 ($L96^{2.53}$ and $C100^{2.57}$), TM3 ($L128^{3.33}$ and $V131^{3.36}$), TM4 ($E182^{4.60}$), TM5 ($F225^{5.46}$) and TM6 ($W284^{6.48}$, $N287^{6.51}$ and $H288^{6.52}$). Among these, mutations $C100^{2.57}$A and $F225^{5.46}$A markedly attenuate DSO-5a (100 μmol/L)-induced signaling, reducing Ca^{2+} mobilization to 58.97% and 18.84%, and IP1 accumulation to 63.35% and 21.92%, respectively, compared to WT BRS3 (100%). Mutations in other residues ($L96^{2.53}$A, $L128^{3.33}$A, $L131^{3.36}$A, $E182^{4.60}$A, $W284^{6.48}$A and $H288^{6.52}$A) nearly abolish DSO-5a-induced IP1 accumulation. Notably, calcium mobilization and IP1 accumulation assays exhibited congruent trends across all mutants, reinforcing the robustness of these structure−function relationships (Fig. 2D and Fig. S6, and Table S3).

The cell surface expression of BRS3 mutants was measured using a FLAG-tag-based flow cytometry assay (Table S2). Fourteen mutants retained substantial surface expression (>70% of WT), indicating that their impaired signaling likely arises from direct effects on ligand recognition or receptor activation rather than deficient membrane localization. Two mutants ($C221^{5.42}$A and $F320^{7.43}$A) exhibited moderate surface expression levels (67.94% and 55.71% of WT, respectively). Three mutants—$F225^{5.46}$A, $H288^{6.52}$A, and $R316^{7.39}$A—showed statistically significant reductions in surface expression (45.34 ± 2.52%, 38.22 ± 3.54%, and 35.57 ± 3.18% of WT, respectively), with attenuated signaling likely reflecting a combination of diminished surface expression and altered ligand affinity or efficacy.

3.4. Recognition of oridonin

Unlike the covalent binding observed with cysteine residues in various target proteins, such as CRM1, PHGDH, and HSP70[42-44], oridonin, does not form covalent bonds with BRS3 but is stabilized within the orthosteric pocket through non-covalent interactions, as shown in our high-resolution cryo-EM structure (Fig. 3A). Oridonin adopts a compact three-dimensional structure, consisting of four all-carbon rings and an oxygen-containing bridge ring (Fig. 3B). Structural analysis revealed that $E182^{4.60}$ and $Y291^{6.55}$ form an intramolecular hydrogen bond, positioning their sidechains above oridonin and thereby constraining its location within the pocket. Additionally, the hydroxyl group at the C7 position of oridonin forms a hydrogen bond with the sidechain amino group of $N287^{6.51}$ and engages in a polar interaction with the imidazole ring of $H288^{6.52}$, further stabilizing its binding (Fig. 3B). Due to aberrant signals being observed in the IP1 accumulation assay with oridonin, only calcium mobilization measurement was employed to study the impact of mutations on BRS3 receptor activity. The $N287^{6.51}$A mutation significantly attenuates oridonin-induced Ca^{2+} mobilization, reducing E_{max} from 100% in WT to 28.63%, whereas the $H288^{6.52}$A nearly abolishes this response (Fig. 3D and Supporting Information Table S4). The hydrophobic residues within the binding pocket contribute notable contact with oridonin. Specifically, the lower region of the binding site aligns with hydrophobic residues, including $L96^{2.53}$, $L128^{3.33}$, $V131^{3.36}$, $F225^{5.46}$, and $F320^{7.43}$ (Fig. 3C). The Ca^{2+} mobilization assay further confirmed that oridonin recognizes

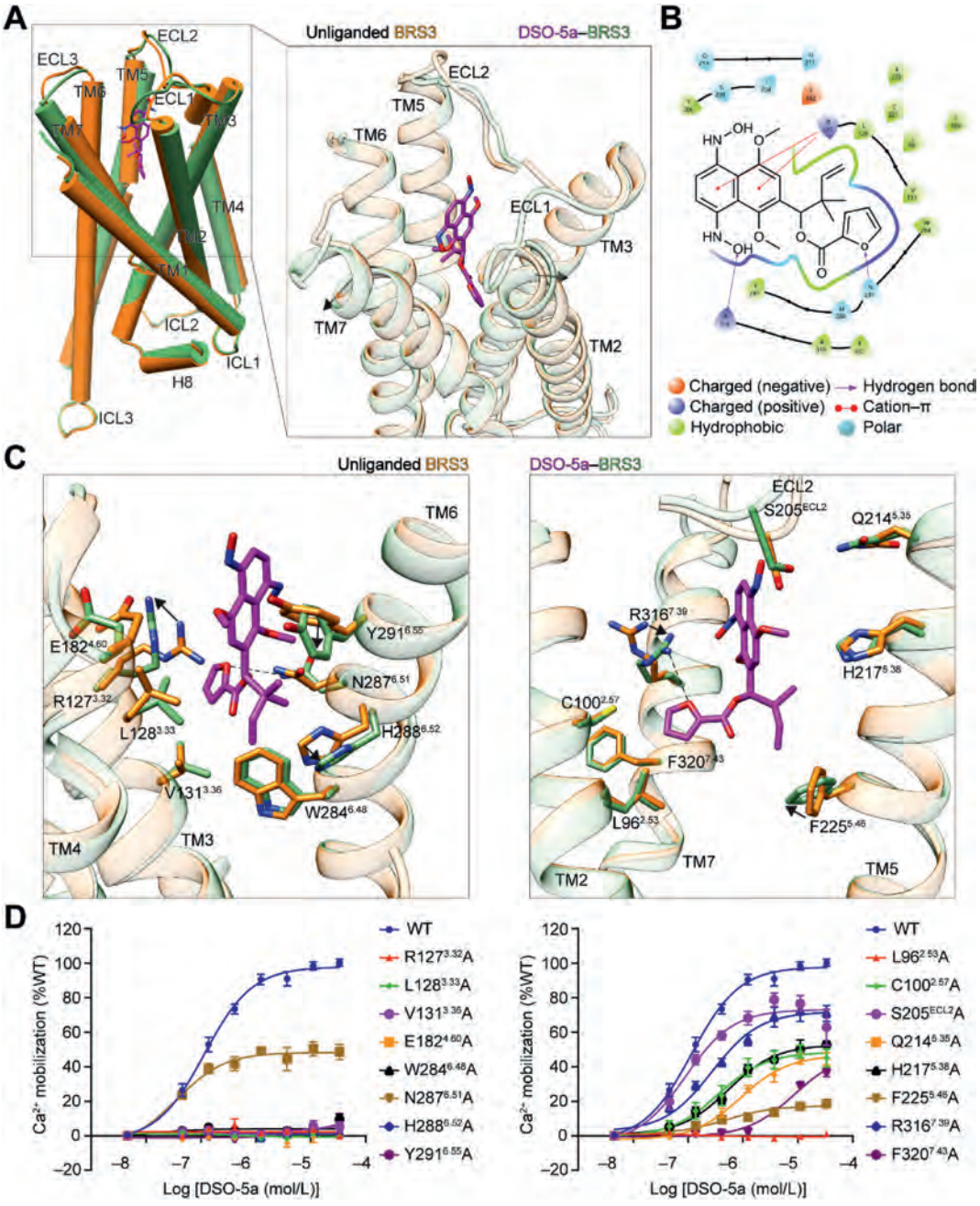

Figure 2 Structural and functional analysis of DSO-5a interaction with BRS3. (A) Superimposition of the unliganded and DSO-5a-bound BRS3 structures. (B) Two-dimensional (2D) diagram of ligand−receptor interaction for DSO-5a. The amino acids of BRS3 residues are highlighted to indicate positive charge (blue), negative charge (red), polar (cyan), and hydrophobic (green). (C) Structural representation of the interaction between DSO-5a and BRS3. Residues involved in DSO-5a (magenta) recognition are shown as sticks and colored green for the DSO-5a-bound BRS3 and orange for the unliganded BRS3 as a reference. Polar contacts are shown as black dashed lines. (D) Effects of BRS3 mutation within the DSO-5a-binding pocket on Ca^{2+} mobilization. BRS3-mediated responses are expressed as percentage: Ca^{2+} mobilization (%WT) = (fluorescence of mutation)/(fluorescence of WT) × 100. Data are presented as mean ± SEM of at least three independent experiments.

and binds to BRS3 through interactions with these hydrophobic residues (Fig. 3D). Unlike DSO-5a, oridonin does not interact with ECL2, suggesting distinct stabilization mechanisms.

3.5. *Activation mechanism*

Structural comparison of BRS3−G_q complexes bound by DSO-5a, oridonin, MK-5046 (PDB code: 8Y53) and BA1 (PDB code: 8Y52)[20], alongside the unliganded structure, demonstrates that BRS3 exhibits a classic active conformation. This is evidenced by the large outward movement of the intracellular halves of TM6, induced by the kink, and the opening of the intracellular crevice, facilitating G protein coupling (Fig. 4)[20]. All four agonists occupy the orthosteric ligand-binding pocket, each establishing a distinct interaction pattern with the extracellular regions of all TMs, except for TM1. For example, oridonin establishes relatively

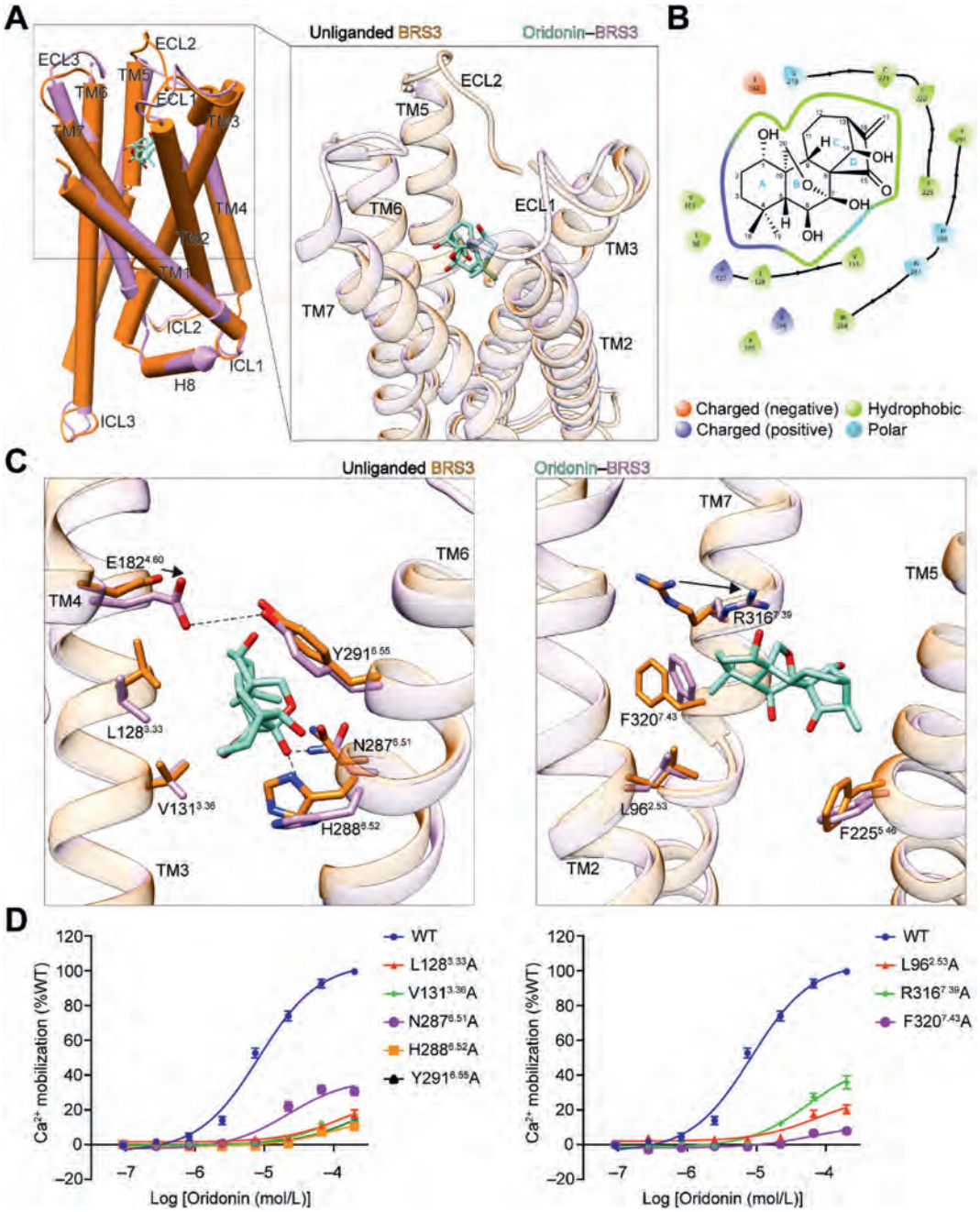

Figure 3 Structural and functional analysis of oridonin interaction with BRS3. (A) Superimposition of the unliganded and oridonin-bound BRS3 structures. (B) 2D diagram of ligand−receptor interaction for oridonin. The amino acids of BRS3 residues are highlighted to indicate positive charge (blue), negative charge (red), polar (cyan), and hydrophobic (green). (C) Structural representation of the interaction between oridonin and BRS3. Residues involved in oridonin recognition are shown as sticks. (D) Effects of BRS3 mutation within the oridonin-binding pocket on Ca^{2+} mobilization. BRS3-mediated responses are expressed as percentage: Ca^{2+} mobilization (%WT) = (fluorescence of mutation)/(fluorescence of WT) × 100. Data are presented as mean ± SEM of at least three independent experiments.

fewer receptor contacts, while BA1 extends fully along the binding pocket, even making contacts with ECLs (Fig. 4A and B). Compared to the MK-5046-bound and BA1-bound BRS3−G_q complexes, the extracellular portion of TM3 in the unliganded and DSO-5a-bound BRS3−G_q complexes shifts outward, while the extracellular part of TM7 moves inward, indicating the ligand-binding pocket adapts specifically to recognize different ligands.

Despite the absence of an orthosteric ligand, the unliganded BRS3−G_q structure closely resembles the four active-state BRS3 structures, particularly the DSO-5a−BRS3−G_q complex (Cα RMSD: 0.92 Å), suggesting an intrinsic conformational plasticity primed for G_q coupling (Fig. 4A−C). These alignments are also reflected at the residue level, especially for activation motifs (Fig. 4D−G). The $D^{3.49}R^{3.50}Y^{3.51}$ and $N^{7.49}P^{7.50}xxY^{7.53}$ ($N^{7.49}P^{7.50}FAL^{7.53}$ in BRS3) motifs are two highly conserved and critical for receptor activation and G protein coupling in class A GPCRs (Fig. 4F)[45,46]. The pre-activated conformation of the unliganded hBRS3−G_q complex provides a structural basis for the

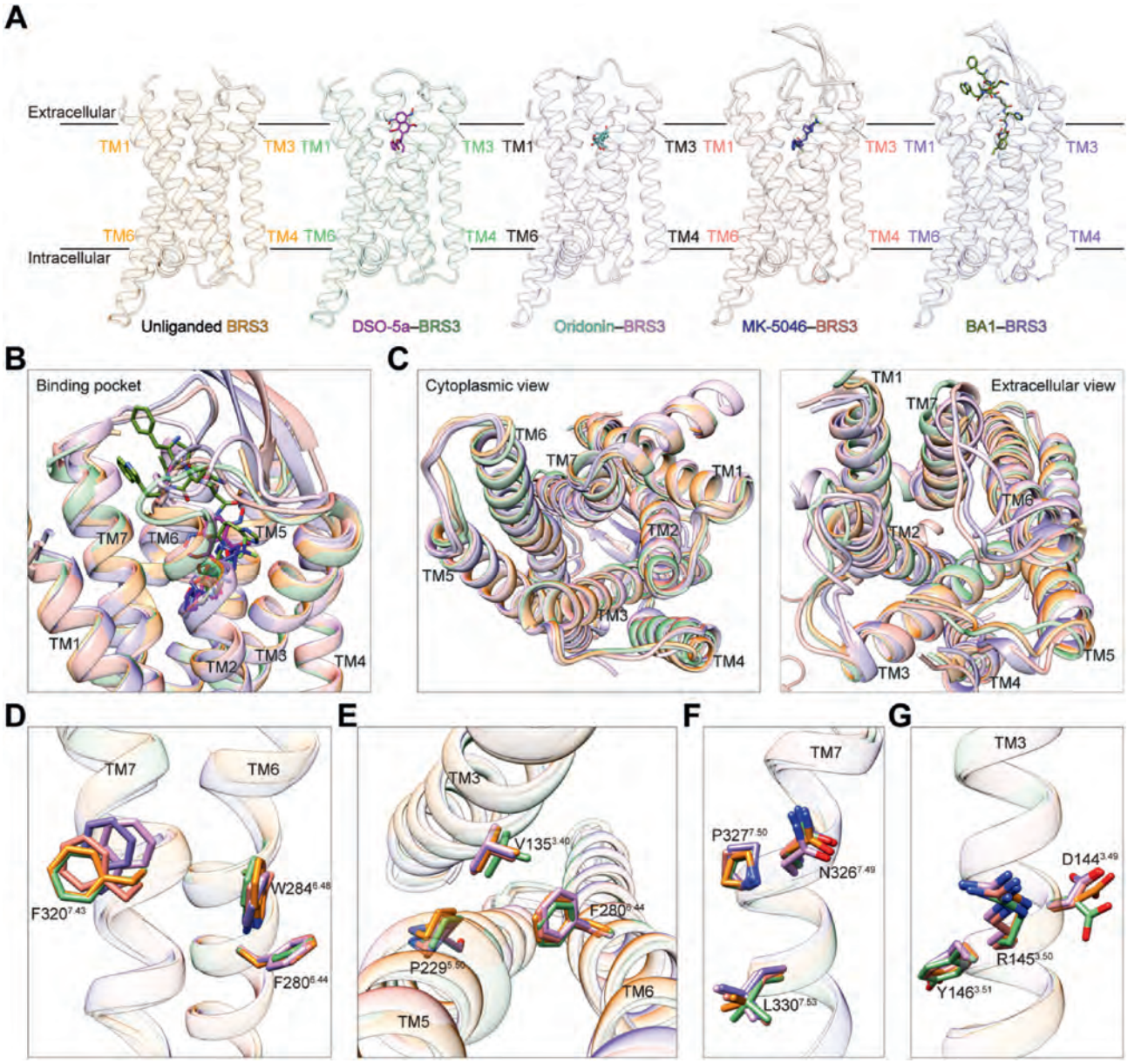

Figure 4 Molecular basis of BRS3 activation. (A) Structural comparison of ligand-binding poses across the DSO-5a-bound, oridonin-bound, MK-5046-bound and BA1-bound BRS3−G_q complexes. (B) Close-up views of the orthosteric binding pocket in the unliganded, DSO-5a-bound, oridonin-bound, MK-5046-bound and BA1-bound BRS3−G_q structures. (C) Cytoplasmic (left) and extracellular (right) views of the BRS3 conformations in distinct agonist-bound state. (D−G) Conformational changes in key micro-switches upon receptor activation, including the toggle switch $F^{6.44}$−$W^{6.48}$−$F^{7.43}$ (D), $P^{5.50}$−$V^{3.40}$−$F^{6.44}$ motif (E), $N^{7.49}P^{7.50}xxL^{7.53}$ motif (F) and $D^{3.49}R^{3.50}Y^{3.51}$ motif (G) across the unliganded and agonist-bound states.

constitutive G_q signaling activity observed in placental mammals, as demonstrated in prior functional studies[6]. In the five complexes, they are nearly superimposed, except for $D144^{3.49}$ that adopts a downward conformation in the unliganded and DSO-5a-bound complexes (Fig. 4G). Mechanistically, agonist binding (synthetic and natural ligands) displaces $W284^{6.48}$, exerting downward force on $F280^{6.44}$ within the $P^{5.50}$-$V^{3.40}$-$F^{6.44}$ triad (Fig. 4D and E). This propagates conformational changes to the $D^{3.49}R^{3.50}Y^{3.51}$ motif (Fig. 4G), triggering intracellular G_q engagement. Despite structural similarities, DSO-5a and oridonin differentially engage transmembrane domain (TMD) residues, suggesting ligand-specific stabilization of the active state. These findings unify the activation pathway of BRS3 across chemically diverse agonists, underscoring its structural adaptability while maintaining functional agonism.

Functional assays revealed that DSO-5a exhibits higher potency than oridonin (pEC_{50} = 6.92 *vs.* 5.08 in calcium mobilization; see Supporting Information Tables S3 and S4, Figs. 2D and 3D). This functional disparity aligns with our cryo-EM structures: DSO-5a engages BRS3 *via* a more extensive interface (918 $Å^2$ *vs.* 668 $Å^2$ for oridonin) and establishes a richer network of polar and stacking interactions across TMs 2−7, whereas oridonin's binding is driven largely by hydrophobic contacts with fewer hydrogen bonds involving TM6 residues. These observations provide a

mechanistic basis for the different binding affinities and efficacies of the two agonists. When looking at other reported agonists (Supporting Information Table S5), BA1, a synthetic nine-amino acid bombesin analog and pan-bombesin receptor agonist[20], exhibits the most extensive interactions (27 pocket residues; interface area: 2030 Å^2). In contrast, MK-5046, a nonpeptide BRS3-selective agonist, maintains high potency (pEC_{50} = 9.3 in IP1 accumulation assay)[20] despite its smaller interface area (824 Å^2), achieved through critical polar and stacking interactions with residues including W284$^{6.48}$, H288$^{6.52}$, Y291$^{6.55}$, and H316$^{7.39}$. These structural and functional distinctions highlight opportunities for optimizing ligand efficiency through further comparative studies.

To further explore the stability and dynamics of the ligand-binding poses, we conducted molecular dynamics (MD) simulations of the unliganded BRS3 receptor and its complexes with DSO-5a and oridonin (Supporting Information Figs. S7 and S8). All systems remained stable during the simulations, as evidenced by consistent RMSD and stable root-mean-square fluctuation (RMSF) profiles (Fig. S7A and S7B). Ligands retained stable occupancy within the binding pocket throughout the trajectories (Fig. S7C and S7D), as supported by stable contacts with pocket residues such as L96$^{2.53}$, R127$^{3.32}$, V131$^{3.36}$, N287$^{6.51}$, and Y291$^{6.55}$ (Fig. S7E and S7F). Notably, differences in ligand−receptor binding modes influenced receptor conformational dynamics, particularly the relative movements of the extracellular ends of TM1, TM2, and TM7 (Fig. S8). In the unliganded state, interhelical distances (TM1−TM2 and TM2−TM7) were lowest during the 500−1000 ns MD simulation window, reflecting a contracted binding pocket due to the absence of agonist binding. Conversely, DSO-5a binding induced the largest separation among these helices, consistent with an expanded pocket. Intriguingly, despite its smaller size compared to the peptide ligand neuromedin B (NMB), oridonin bound deeper within the pocket and selectively maintained the TM1−TM2 separation, but not TM1−TM7 and TM2−TM7 (Fig. S8E−S8G).

3.6. *G protein coupling*

As shown in Fig. 5A, the α5 helix of Gα_q aligns closely between the unliganded and DSO-5a-bound BRS3−G$_q$ complexes and inserts into the cytoplasmic cavity of the receptor TMD. This insertion establishes multiple polar contacts including one hydrogen bond between R266$^{6.30}$ in BRS3 and D233 in the α5 helix. Meanwhile, there is an additional hydrogen bond between D144$^{3.49}$ and Y243 only observed in the DSO-5a−BRS3−G$_q$ complex, due to the distinct orientation of the sidechains of D144$^{3.49}$ (Fig. 5B).

Furthermore, the Gα_q αN helix in the DSO-5a−BRS3−G$_q$ complex shifts by 2.6 Å towards Gβ (measured at the Cα atoms of A7), compared to the unliganded form (Fig. 5C and D). Consequently, the ICL2 residue R155^{ICL2} interacts closely with the αN

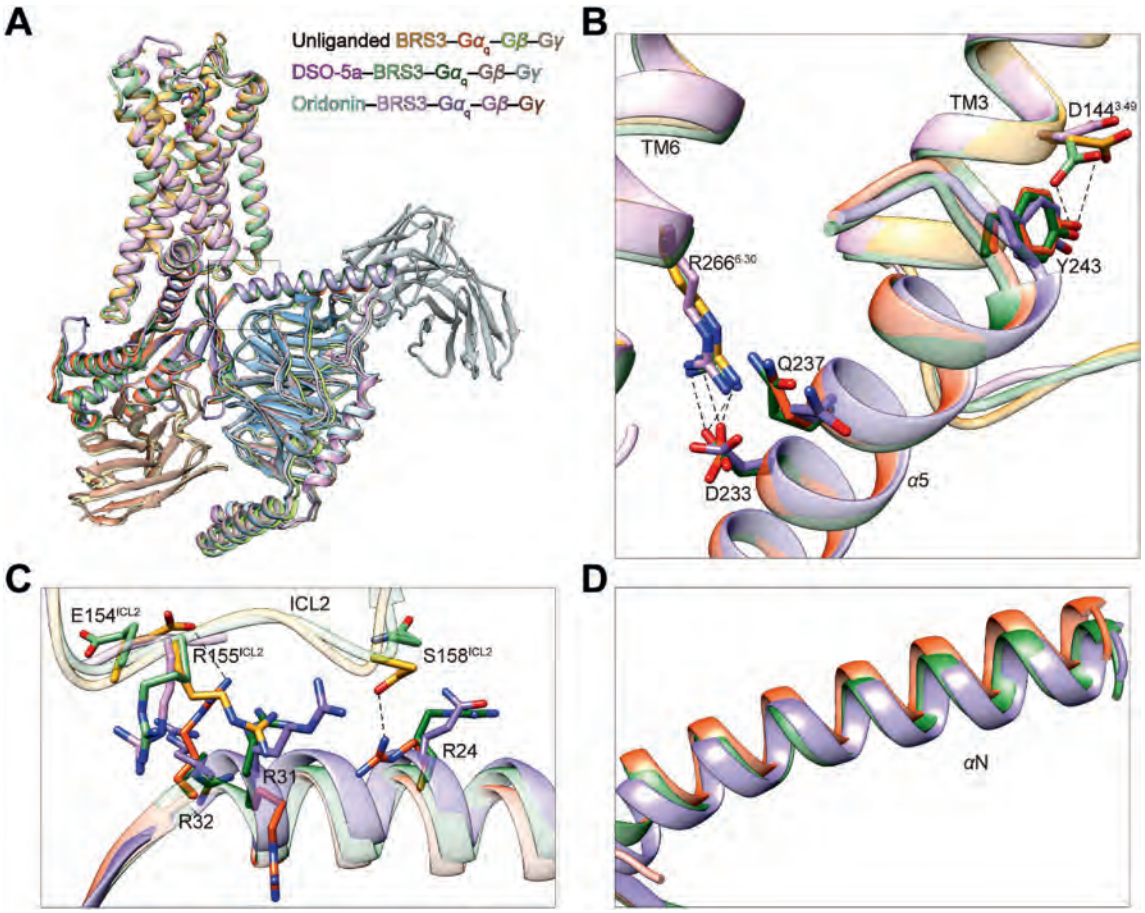

Figure 5 G protein coupling of BRS3 across the unliganded and agonist-bound states. (A) Structural alignment of the unliganded, DSO-5a-bound and oridonin-bound BRS3−G$_q$ complexes. (B, C) Structural comparison of the α5 helix (B) and αN helix (C) of Gα_q across the three BRS3−G$_q$ complexes. Polar contacts are shown as black dashed lines. (D) Overall comparison of the αN helix of Gα_q in the three complexes.

helix in $G\alpha_q$, allowing for the formation of a salt bridge between $E154^{ICL2}$ and R32 in the αN helix of $G\alpha_q$, as observed in the unliganded structure (Fig. 5C)[47]. Meanwhile, $S158^{ICL2}$ rotates downward to form a hydrogen bond with R24 in the αN helix. Both contacts are absent in the DSO-5a−BRS3−G_q complex, implicating ligand-induced conformational rearrangements in ICL2.

4. Discussion

BRS3, a GPCR involved in energy homeostasis and glucose metabolism, has been structurally characterized in both unliganded and active states bound by two Chinese herb-derived agonists, DSO-5a and oridonin. High-resolution cryo-EM structures offer novel insights into ligand recognition and receptor activation. Although DSO-5a and oridonin bind to the same orthosteric pocket as synthetic agonists like MK-5046 and BA1, they interact with distinct receptor residues, highlighting the conformational flexibility of BRS3 in recognizing different ligands. Specifically, DSO-5a stabilizes an active conformation through polar and stacking interactions, akin to synthetic agonists, whereas oridonin induces a unique binding mode, predominantly involving hydrophobic contacts. The structural observations are supported by mutagenesis results, which link specific receptor residues to ligand efficacy and receptor activation. Together, these findings expand our understanding of how BRS3 can be modulated by bioactive natural products and their derivatives, offering a structural framework for translational applications.

The unliganded BRS3 structure adopts a pre-activated conformation that closely resembles the agonist-bound state, suggesting an intrinsic conformational plasticity that primes the receptor for G_q coupling[48]. This pre-activation may drive BRS3's high constitutive activity, which is physiologically critical for BRS3's role in regulating energy balance, regulate body temperature, energy expenditure, and heart rate[6,7]. Ligand binding triggers specific rearrangements in the TMs and the repositions of key residues such as $D144^{3.49}$, $R155^{ICL2}$ and $S158^{ICL2}$. Regardless of the presence of a ligand, receptor activation follows defined movements, involving the displacement of $W284^{6.48}$, progressing through the $D^{3.49}R^{3.50}Y^{3.51}$ and $N^{7.49}P^{7.50}xxY^{7.53}$ motifs *via* the $P^{5.50}$−$V^{3.40}$−$F^{6.44}$ triad and the hydrophobic patch[20], finally BRS3 can stably engage with the G_q. This pre-activated state may explain the basal activity of BRS3.

Recognition of DSO-5a and oridonin by BRS3 highlights how Chinese herb-derived agonists utilize distinct pharmacophores to induce receptor activation. DSO-5a, a dimethyl shikonin oxime derivative, adopts a "Y"-shaped conformation within the BRS3 orthosteric pocket, similar to MK-5046[20]. It forms extensive polar and nonpolar interactions with residues in TMs 2−7, as well as ECL2. In contrast, oridonin, a diterpenoid, adopts a compact structure and predominantly interacts through hydrophobic contacts, with fewer hydrogen bonds involving residues in TM6. These binding modes underscore the molecular specificity with which Chinese herb-derived compounds modulate BRS3 activity. Their distinct receptor−ligand interaction patterns align with their pharmacological profiles in calcium mobilization assays, where DSO-5a demonstrates significantly higher potency (pEC_{50} = 6.92) compared to oridonin (pEC_{50} = 5.08). The high-resolution cryo-EM structure provides a framework for optimizing oridonin's potency by guiding strategic modifications to its functional groups, such as enhancing polar interactions at key interfacial residues while preserving its natural core scaffold.

The cryo-EM structure of BRS3 in complex with DSO-5a provides critical insights for rational drug design, integrating mutagenesis data and structure−activity relationship (SAR) studies of synthesized derivatives[11]. Taken the furanyl moiety of DSO-5a for example, it engages cation−π interactions with $R127^{3.32}$ and π−π stacking with $W284^{6.48}$, forms hydrogen bonds with $N287^{6.51}$ and $R316^{7.39}$, while its hydrophobic contacts with $L96^{2.53}$ and $V131^{3.36}$ further stabilize binding. SAR studies confirm that aromatic substitutions at this site retain agonist potency in the IP1 assay: replacing furanyl (DSO-5a, pEC_{50} = 8.422) with phenyl (DSO-5h, pEC_{50} = 8.320) preserves activity, whereas bulkier or polar groups [*e.g.*, isovaleryl (DSO-5l, pEC_{50} = 7.280), 2-pyridyl (DSO-5c, pEC_{50} = 7.833), or saturated 2-tetrahydrofuranyl (DSO-5b, pEC_{50} = 6.871)] reduce the potency, likely due to steric clashes or disrupted interactions. Similarly, modifications to the phenyl rings of DSO-5h, such as adding methyl (DSO-5i, pEC_{50} = 7.088) or electron-withdrawing carbonyl groups (DSO-5j, pEC_{50} = 6.507), diminish the activity, reflecting the limited cavity volume in this region. Notably, the dimethyl groups of DSO-5a occupy the TM3−TM5 cleft near $H217^{5.38}$ and the TM6 interface proximal to $N287^{6.51}$, but neither forms polar contacts, suggesting opportunities to enhance agonism by introducing hydrogen-bond donors or acceptors at these positions. Our findings collectively highlight strategies for optimizing BRS3 modulators: preserving critical interactions at the furanyl-shikonin site, minimizing steric bulk in constrained regions, and leveraging underutilized polar interfaces near TM3−TM5 and TM6 for functional group engineering. Future studies combining structural-guided design with medicinal chemistry could refine agonist specificity and potency for developing new therapeutics against metabolic disease.

5. Conclusions

In summary, this study provides detailed structural insights into the molecular recognition and activation mechanisms of BRS3 by DSO-5a and oridonin, two TCM-derived ligands. These findings not only deepen our understanding of the activation mechanism of BRS3 but also lay the foundation for the discovery of novel BRS3-targeted therapeutic agents from natural resources.

Acknowledgments

We thank Zhaotong Cong, Wenbo Feng and Jianzheng Zhu for valuable discussion. The cryo-EM data were collected at the Cryo-Electron Microscopy Research Center and Shanghai Advanced Electron Microscope Center, Shanghai Institute of Materia Medica, Chinese Academy of Sciences. This work was partially supported by the National Natural Science Foundation of China 82273961 (Ming-Wei Wang), 82073904 (Ming-Wei Wang, China), 81872915 (Ming-Wei Wang, China), 32171189 (Wanchao Yin, China), 32130022 (H. Eric Xu, China) and 82121005 (H. Eric Xu, China); the National Key R&D Program of China 2022YFA1302900 (Wanchao Yin) and 2022YFC2703105 (H. Eric Xu, China); the Youth Innovation Promotion Association of CAS 2021278 (Wanchao Yin, China); Zhongshan Municipal Bureau of Science and Technology CXTD2023010 (Wanchao Yin, China); High-Level New R&D Institute 2019B090904008 (Wanchao Yin, China); High-level Innovative Research Institute from Department

of Science and Technology of Guangdong Province 2021B0909050003 (Wanchao Yin, China); CAS Strategic Priority Research Program XDB37030103 (H. Eric Xu, China); Shanghai Municipal Science and Technology Major Project 2019SHZDZX02 (H. Eric Xu, China); the Lingang Laboratory Grant No. LG-GG-202204-01 (H. Eric Xu, China); STI2030-Major Project 2021ZD0203400 (Qingtong Zhou, China); and Hainan Provincial Major Science and Technology Project ZDKJ2021028 (Qingtong Zhou, China).

Author contributions

Jie Li, Changyao Li, Qingtong Zhou, Wei Han, Youwei Xu, Yiting Mai and Yan Zhang performed research; Jie Li, Changyao Li, Qingtong Zhou, Wei Han, Wanchao Yin and Ming-Wei Wang analyzed the data; Jiahua Cui provided DSO-5a; Mingzhu Fang conducted calcium mobilization assay and analyzed the results with Yan Zhang; Jie Li, Changyao Li, Qingtong Zhou, Wei Han, and Ming-Wei Wang wrote the manuscript with inputs from all co-authors; H. Eric Xu, Yan Zhang, Wanchao Yin and Ming-Wei Wang initiated the project; Wanchao Yin and Ming-Wei Wang supervised the studies.

Data and materials availability

All relevant data are available from the authors and/or included in the manuscript or Supporting Information The atomic coordinates have been deposited in the Protein Data Bank (PDB) under accession codes: 9LWP [unliganded BRS3−G_q], 9K07 [DSO-5a−BRS3−G_q] and 9M0J [oridonin−BRS3−G_q], and the electron microscopy maps have been deposited in the Electron Microscopy Data Bank (EMDB) under accession codes: EMD-63455 [unliganded BRS3−G_q], EMD-61941 [DSO-5a−BRS3−G_q] and EMD-63545 [oridonin−BRS3−G_q].

Conflicts of interest

All the authors declare no conflicts of interest.

Appendix A. Supporting information

Supporting information to this article can be found online at https://doi.org/10.1016/j.apsb.2025.06.025.

References

1. Zhang L, Parks GS, Wang Z, Wang L, Lew M, Civelli O. Anatomical characterization of bombesin receptor subtype-3 mRNA expression in the rodent central nervous system. *J Comp Neurol* 2013;**521**:1020−39.
2. Regard JB, Sato IT, Coughlin SR. Anatomical profiling of G protein-coupled receptor expression. *Cell* 2008;**135**:561−71.
3. Yamada K, Santo Yamada Y, Wada E, Wada K. Role of bombesin (BN)-like peptides/receptors in emotional behavior by comparison of three strains of BN-like peptide receptor knockout mice. *Mol Psychiatr* 2002;**7**:113−6.
4. Ladenheim EE, Hamilton NL, Behles RR, Bi S, Hampton LL, Battey JF, et al. Factors contributing to obesity in bombesin receptor subtype-3-deficient mice. *Endocrinology* 2008;**149**:971−8.
5. Guan XM, Chen H, Dobbelaar PH, Dong Y, Fong TM, Gagen K, et al. Regulation of energy homeostasis by bombesin receptor subtype-3: selective receptor agonists for the treatment of obesity. *Cell Metab* 2010;**11**:101−12.
6. Tang H, Shu C, Chen H, Zhang X, Zang Z, Deng C. Constitutively active BRS3 is a genuinely orphan GPCR in placental mammals. *PLoS Biol* 2019;**17**:e3000175.
7. Pinol RA, Zahler SH, Li C, Saha A, Tan BK, Skop V, et al. Brs3 neurons in the mouse dorsomedial hypothalamus regulate body temperature, energy expenditure, and heart rate, but not food intake. *Nat Neurosci* 2018;**21**:1530−40.
8. Nakamichi Y, Wada E, Aoki K, Ohara Imaizumi M, Kikuta T, Nishiwaki C, et al. Functions of pancreatic beta cells and adipocytes in bombesin receptor subtype-3-deficient mice. *Biochem Biophys Res Commun* 2004;**318**:698−703.
9. Gu X, Hao D, Xiao P. Research progress of Chinese herbal medicine compounds and their bioactivities: fruitful 2020. *Chin Herb Med* 2022;**14**:171−86.
10. Zhu Y, Wu L, Zhao Y, Wang Z, Lu J, Yu Y, et al. Discovery of oridonin as a novel agonist for BRS-3. *Phytomedicine* 2022;**100**:154085.
11. Wu L, Cui J, Zhao C, Wang Z, Lu J, Li S, et al. Discovery of dimethyl shikonin oxime 5a, a potent, selective bombesin receptor subtype-3 agonist for the treatment of type 2 diabetes mellitus. *J Med Chem* 2023;**66**:8011−29.
12. Cui J, Zhang X, Huang G, Zhang Q, Dong J, Sun G, et al. DMAKO-20 as a new multitarget anticancer prodrug activated by the tumor specific CYP1B1 enzyme. *Mol Pharm* 2019;**16**:409−21.
13. Auber RP, Suttiyut T, McCoy RM, Ghaste M, Crook JW, Pendleton AL, et al. Hybrid *de novo* genome assembly of red gromwell (*Lithospermum erythrorhizon*) reveals evolutionary insight into shikonin biosynthesis. *Hortic Res* 2020;**7**:82.
14. Lateef DM, Xiao C, Brychta RJ, Diedrich A, Schnermann J, Reitman ML. Bombesin-like receptor 3 regulates blood pressure and heart rate *via* a central sympathetic mechanism. *Am J Physiol Heart Circ Physiol* 2016;**310**:H891−8.
15. Yang YC, Wei MC, Huang TC. Optimisation of an ultrasound-assisted extraction followed by RP-HPLC separation for the simultaneous determination of oleanolic acid, ursolic acid and oridonin content in *Rabdosia rubescens*. *Phytochem Anal* 2012;**23**:627−36.
16. Yao Z, Xie F, Li M, Liang Z, Xu W, Yang J, et al. Oridonin induces autophagy *via* inhibition of glucose metabolism in p53-mutated colorectal cancer cells. *Cell Death Dis* 2017;**8**:e2633.
17. Yu T, Xie W, Sun Y. Oridonin inhibits LPS-induced inflammation in human gingival fibroblasts by activating PPARgamma. *Int Immunopharmacol* 2019;**72**:301−7.
18. Jia T, Cai M, Ma X, Li M, Qiao J, Chen T. Oridonin inhibits IL-1beta-induced inflammation in human osteoarthritis chondrocytes by activating PPAR-gamma. *Int Immunopharmacol* 2019;**69**:382−8.
19. Xu L, Bi Y, Xu Y, Zhang Z, Xu W, Zhang S, et al. Oridonin inhibits the migration and epithelial-to-mesenchymal transition of small cell lung cancer cells by suppressing FAK-ERK1/2 signalling pathway. *J Cell Mol Med* 2020;**24**:4480−93.
20. Li C, Xu Y, Su W, He X, Li J, Li X, et al. Structural insights into ligand recognition, selectivity, and activation of bombesin receptor subtype-3. *Cell Rep* 2024;**43**:114511.
21. Chun E, Thompson AA, Liu W, Roth CB, Griffith MT, Katritch V, et al. Fusion partner toolchest for the stabilization and crystallization of G protein-coupled receptors. *Structure* 2012;**20**:967−76.
22. Fan S, Li J, Zhuang J, Zhou Q, Mai Y, Lin B, et al. Disulfide-directed multicyclic peptides with N-terminally extendable alpha-helices for recognition and activation of g protein-coupled receptors. *J Am Chem Soc* 2025;**147**:4821−32.
23. Chen Y, Zhou Q, Wang J, Xu Y, Wang Y, Yan J, et al. Ligand recognition mechanism of the human relaxin family peptide receptor 4 (RXFP4). *Nat Commun* 2023;**14**:492.
24. Kim K, Che T, Panova O, DiBerto JF, Lyu J, Krumm BE, et al. Structure of a hallucinogen-activated Gq-coupled 5-HT_{2A} serotonin receptor. *Cell* 2020;**182**. 1574-88.e19.

25. Nehme R, Carpenter B, Singhal A, Strege A, Edwards PC, White CF, et al. Mini-G proteins: novel tools for studying GPCRs in their active conformation. *PLoS One* 2017;**12**:e0175642.
26. Liu P, Jia MZ, Zhou XE, De Waal PW, Dickson BM, Liu B, et al. The structural basis of the dominant negative phenotype of the $G\alpha_{i1}\beta_1\gamma_2$ G203A/A326S heterotrimer. *Acta Pharmacol Sin* 2016;**37**:1259−72.
27. Kang Y, Kuybeda O, de Waal PW, Mukherjee S, Van Eps N, Dutka P, et al. Cryo-EM structure of human rhodopsin bound to an inhibitory G protein. *Nature* 2018;**561**:E44.
28. Maeda S, Qu Q, Robertson MJ, Skiniotis G, Kobilka BK. Structures of the M1 and M2 muscarinic acetylcholine receptor/G-protein complexes. *Science* 2019;**364**:552−7.
29. Rasmussen SG, DeVree BT, Zou Y, Kruse AC, Chung KY, Kobilka TS, et al. Crystal structure of the beta2 adrenergic receptor-Gs protein complex. *Nature* 2011;**477**:549−55.
30. Li C, Xu Y, Liu H, Cai H, Jiang Y, Xu HE, et al. Molecular recognition of itch-associated neuropeptides by bombesin receptors. *Cell Res* 2023;**33**:184−7.
31. Pettersen EF, Goddard TD, Huang CC, Couch GS, Greenblatt DM, Meng EC, et al. UCSF Chimera—a visualization system for exploratory research and analysis. *J Comput Chem* 2004;**25**:1605−12.
32. Meng EC, Goddard TD, Pettersen EF, Couch GS, Pearson ZJ, Morris JH, et al. UCSF ChimeraX: tools for structure building and analysis. *Protein Sci* 2023;**32**:e4792.
33. Emsley P, Cowtan K. Coot: model-building tools for molecular graphics. *Acta Crystallogr D Biol Crystallogr* 2004;**60**:2126−32.
34. Adams PD, Afonine PV, Bunkoczi G, Chen VB, Davis IW, Echols N, et al. PHENIX: a comprehensive Python-based system for macromolecular structure solution. *Acta Crystallogr D Biol Crystallogr* 2010; **66**:213−21.
35. Abraham MJ, Murtola T, Schulz R, Páll S, Smith JC, Hess B, et al. GROMACS: high performance molecular simulations through multi-level parallelism from laptops to supercomputers. *SoftwareX* 2015; **1**−**2**:19−25.
36. Sastry GM, Adzhigirey M, Day T, Annabhimoju R, Sherman W. Protein and ligand preparation: parameters, protocols, and influence on virtual screening enrichments. *J Comput Aided Mol Des* 2013;**27**:221−34.
37. Lee J, Cheng X, Swails JM, Yeom MS, Eastman PK, Lemkul JA, et al. CHARMM-GUI input generator for NAMD, GROMACS, AMBER, OpenMM, and CHARMM/OpenMM simulations using the CHARMM36 additive force field. *J Chem Theor Comput* 2016;**12**: 405−13.
38. Huang J, Rauscher S, Nawrocki G, Ran T, Feig M, de Groot BL, et al. CHARMM36m: an improved force field for folded and intrinsically disordered proteins. *Nat Methods* 2017;**14**:71−3.
39. Vanommeslaeghe K, Hatcher E, Acharya C, Kundu S, Zhong S, Shim J, et al. CHARMM general force field: a force field for drug-like molecules compatible with the CHARMM all-atom additive biological force fields. *J Comput Chem* 2010;**31**:671−90.
40. Hess B. P-LINCS: a parallel linear constraint solver for molecular simulation. *J Chem Theor Comput* 2008;**4**:116−22.
41. Aoki KM, Yonezawa F. Constant-pressure molecular-dynamics simulations of the crystal-smectic transition in systems of soft parallel spherocylinders. *Phys Rev A* 1992;**46**:6541−9.
42. Lei Y, Li Y, Tan Y, Qian Z, Zhou Q, Jia D, et al. Novel mechanistic observations and NES-binding groove features revealed by the CRM1 inhibitors plumbagin and oridonin. *J Nat Prod* 2021;**84**:1478−88.
43. Tan Y, Zhou X, Gong Y, Gou K, Luo Y, Jia D, et al. Biophysical and biochemical properties of PHGDH revealed by studies on PHGDH inhibitors. *Cell Mol Life Sci* 2021;**79**:27.
44. Dal Piaz F, Cotugno R, Lepore L, Vassallo A, Malafronte N, Lauro G, et al. Chemical proteomics reveals HSP70 1A as a target for the anticancer diterpene oridonin in Jurkat cells. *J Proteomics* 2013;**82**: 14−26.
45. Zhou Q, Yang D, Wu M, Guo Y, Guo W, Zhong L, et al. Common activation mechanism of class A GPCRs. *eLife* 2019;**8**:e50279.
46. Weis WI, Kobilka BK. The molecular basis of g protein-coupled receptor activation. *Annu Rev Biochem* 2018;**87**:897−919.
47. Duan J, Shen DD, Zhao T, Guo S, He X, Yin W, et al. Molecular basis for allosteric agonism and G protein subtype selectivity of galanin receptors. *Nat Commun* 2022;**13**:1364.
48. Cong Z, Zhao F, Li Y, Luo G, Mai Y, Chen X, et al. Molecular features of the ligand-free GLP-1R, GCGR and GIPR in complex with G_s proteins. *Cell Discov* 2024;**10**:18.